

GT2017-64466

MULTIDISCIPLINARY DESIGN OF A THREE STAGE HIGH SPEED BOOSTER

Marcus Lejon*

Department of Applied Mechanics
Chalmers University of Technology
Gothenburg, Sweden
Email: marcus.lejon@chalmers.se

Tomas Grönstedt

Department of Applied Mechanics
Chalmers University of Technology
Gothenburg, Sweden

Nenad Glodic

Paul Petrie-Repar
Department of Energy Technology
Royal Institute of Technology
Stockholm, Sweden

Magnus Genrup

Department of Energy Sciences
Lund University
Lund, Sweden

Alexander Mann

Dep. of Industrial Manufacturing Methods
Swerea IVF
Gothenburg, Sweden

ABSTRACT

The paper describes a multidisciplinary conceptual design of an axial compressor, targeting a three stage, high speed, high efficiency booster with a design pressure ratio of 2.8. The paper is outlined in a step wise manner starting from basic aircraft and engine thrust requirements, establishing the definition of the high speed booster interface points and its location in the engine. Thereafter, the aerodynamic 1D/2D design is carried out using the commercial throughflow tool SC90C. A number of design aspects are described, and the steps necessary to arrive at the final design are outlined. The SC90C based design is then carried over to a CFD based conceptual design tool AxCent, in which a first profiling is carried out based on a multiple circular arc blade definition. The design obtained at this point is referred to as the VINK compressor. The first stage of the compressor is then optimized using an in-house optimization tool, where the objective functions are evaluated from detailed CFD calculations. The design is improved in terms of efficiency and in terms of meeting the design criteria put on the stage in the earlier design phases. Finally, some aeromechanical design aspects of the first stage are considered. The geometry and inlet boundary conditions of

the compressor are shared with the turbomachinery community on a public server. This is intended to be used as a test case for further optimization and analysis.

NOMENCLATURE

C	Velocity in absolute frame of reference
C_p	Static pressure recovery coefficient
M	Mach number
T	Temperature
W	Work
L	Blade span
fa	fuel air ratio
h_{max}	Maximum blade mode shape amplitude
h_0	Stagnation enthalpy
\dot{m}	Mass flow
n	Rotational speed
p	Pressure
s	Pitch

* Address all correspondence to this author.

Abbreviations

AR	Aspect ratio
CFD	Computational fluid dynamics
GA	Genetic algorithm
HPC	High pressure compressor
ICC	Intermediate compressor channel
ISA	International standard atmosphere
LHS	Latin hypercube sampling
LPT	Low pressure turbine
MCA	Multiple circular arc
R1	Rotor 1
S1	Stator 1
SM	Surge margin
NSGA-II	Non-dominated sorting genetic algorithm II
RBF	Radial basis function
URANS	Unsteady Reynolds averaged Navier Stokes
VIGV	Variable inlet guide vane
rpm	Revolutions per minute

Subscripts

0	Stagnation condition
m	Meridional
ref	Reference

Greek

β	Relative flow angle
η_p	Polytropic efficiency
ω	Loss coefficient
ϕ	Flow function, C_m/U
ψ	Stage loading, h_0/U^2
π	Pressure ratio
Ξ	Aerodynamic damping coefficient

INTRODUCTION

The 3D virtual design of a high speed booster is outlined in this work, starting almost from a clean slate. Some initial assumptions are made on the airframe and engine architecture. This leads on to engine thrust requirements being established at a number of operating points. Conceptual 1D/2D design is then followed by 3D aerodynamic design, optimization and finally also an assessment of some aeromechanical aspects of the design. The design approach is captured by the traditional “successive refinement” illustrated in Fig. 1.

One aim of this “chain-of-design iterations” working style is to demonstrate that, within a network of Swedish universities (Chalmers, KTH and LTH), the joint capability to perform the necessary steps leading to a 3D definition of a high speed compressor can be achieved. Cross-university collaborative efforts of this nature are strategically critical for a small country like Sweden [1].

At the onset of the project, studying a range of engine architectures and compressor designs covering these architectures

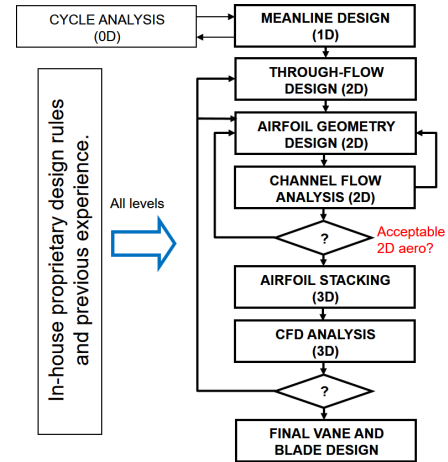


FIGURE 1. AXIAL TYPE TURBOMACHINERY DESIGN LOOP

was discussed. However, due to the long term outlook for aero engines, a geared engine concept was chosen as the basic architecture. It could be argued that a geared engine can capture most of the efficiency advantages that an open rotor architecture can provide, albeit that some of the benefits in increased propulsive efficiency are unlikely to be captured even with very mature geared engine designs [2]. In addition, the geared architecture would require substantially fewer parts [3] and hence be more cost efficient. Notable early efforts on geared engine concepts are represented by the Honeywell engines TFE731 (originally Garrett) and the ALF 502 (developed in collaboration with Lycoming and Allied Signal). More recently, this architecture has been championed predominantly by Pratt Whitney. Notably, for future engine designs, the geared option is also being considered by Rolls-Royce for the long term development [4]. Taking a longer time perspective, *e.g.* a year 2050 vision, open rotor architectures are more likely to be a feasible alternative for shorter range operations [5] due to a larger part of the mission being operated at lower flight speeds. Hence, it is likely that high speed boosters targeting geared architectures will receive considerable attention in future design programs.

Although the list of design studies on axial compressors is extensive in the literature, see *e.g.* [6–11], work describing the chain of steps, from cycle definition to 3D aero optimization and aeromechanical analysis, is quite scarce. In addition, compressor geometry is usually only shared partially, either deliberately or because of limitations in how detailed a geometry can be represented in paper form. For this reason the final geometry of the resulting optimization is shared on a public server [12], intended to be used as a test case for further optimization and analysis.

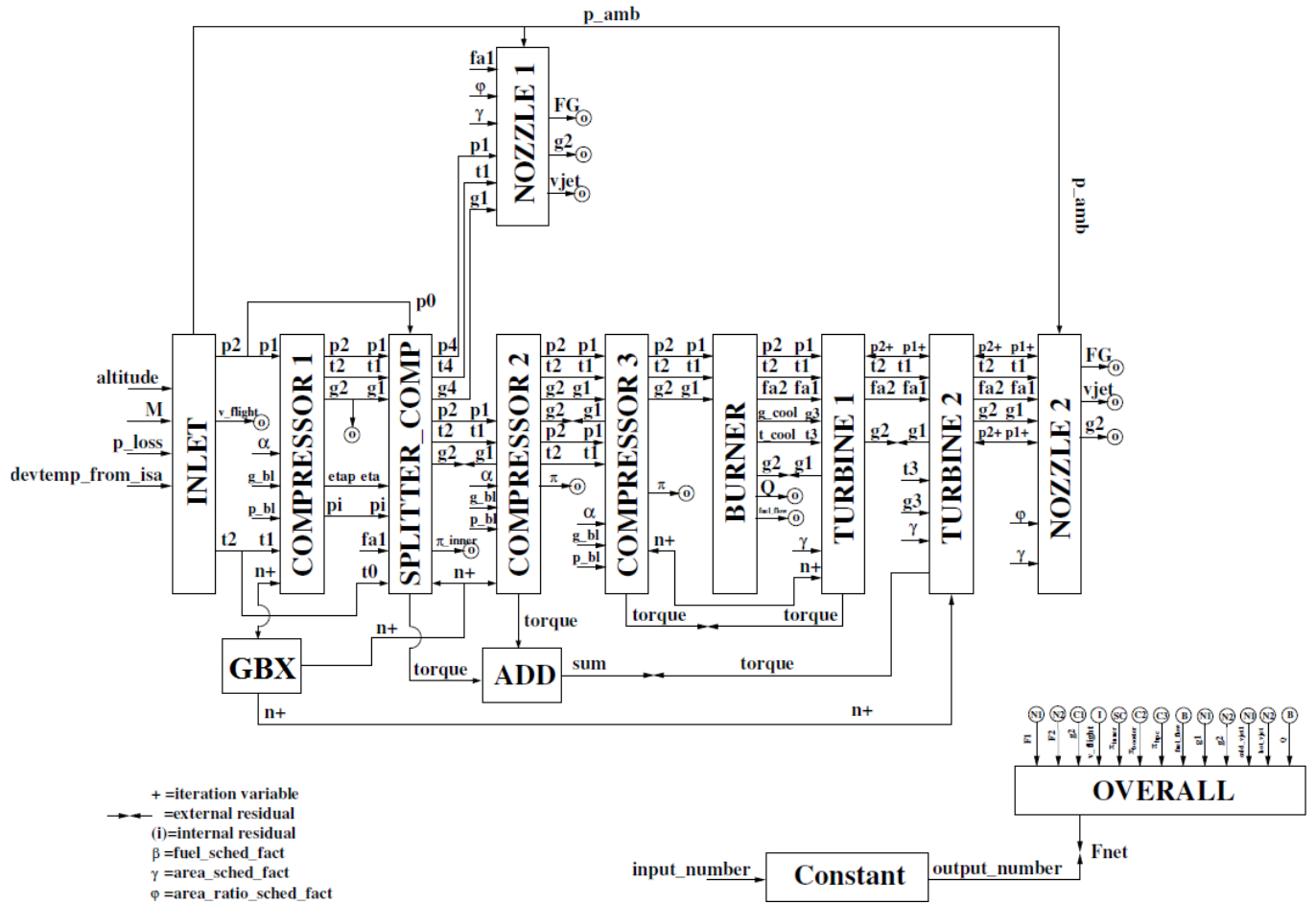


FIGURE 2. WIRING DIAGRAM FOR GEARED ENGINE ARCHITECTURE, USING GESTPAN DATA DEFINITIONS [13]

HIGH SPEED BOOSTER DESIGN PROCESS

Cycle Definition and Compressor Interface

An airframe set of requirements needs to be available to define requirements for an engine. Since it was outside the scope of this project to actively consider airframe alternatives, an existing definition with which Chalmers had experience was selected. The cycle targets a twin aisle, two engine aircraft targeting a 70 klb thrust at static conditions. Assumptions on turbomachinery efficiencies are in line with previously published work [14].

From the basic thrust definition stated above, as well as the selected geared engine architecture, a range of performance data must be established for the engine. As a part of this work, the high speed booster needs to be defined at a number of operating conditions. The Chalmers in-house tool GESTPAN [13] was

used to obtain the performance data needed to start the 1D design of the high speed booster. A schematic of the engine configuration is shown in Fig. 2.

An aerodynamically relatively lightly loaded, high efficiency three stage design was targeted. Top-of-climb performance data for the booster were set as design conditions. The key performance data are given in Table 1. Early designs targeted an even lower pressure ratio of 2.5, but this loading was actually so low that it carried an efficiency penalty. A pressure ratio of 2.8 was ultimately chosen for the booster.

The selection of rotational speed was evaluated against fan and low pressure turbine performance. In top-of-climb, the 115 inch diameter fan pressure ratio was 1.49 operating at a tip speed of 321 m/s. The blade speeds for the four stage low pressure turbine (LPT) were set to 337, 352, 366 and 377 m/s respectively.

TABLE 1. HIGH SPEED BOOSTER PERFORMANCE DATA

Parameter	Value
$p_{0,23}$ [kPa]	46.69
$T_{0,23}$ [K]	282.4
$\dot{m}_{0,23}$ [kg/s]	42.68
π	2.80
n [rpm]	6242.0
Deviation from ISA	+10 K
Cruise altitude	35 kft

Throughflow design and SC90C

The SC90C program [15] is a streamline curvature based program suitable for conceptual aerodynamic design of axial compressors. For the three stage booster studied in this work, a number of design parameters have been explored to find suitable designs. Stage pressure ratio, radial variation in pressure ratio, interstage and inlet guide vane swirl distribution, hub and shroud line definition as well as selection of the number of blades were simultaneously explored to find a good initial throughflow design.

To facilitate defining the initial design, an in-house Python program was developed to interface with the input and output ASCII text files that the SC90C program uses. The target of this first throughflow design exercise was to provide a feasible design rather than an optimal design. It is viewed that throughflow loss model based programs do not capture sufficient physics to provide a meaningful environment for extended optimization. Rather, they provide opportunity to define an initial compressor geometry definition that fulfills a number of conflicting requirements having a range of parameters well within recommended

TABLE 2. INITIAL THROUGHFLOW BASED BOOSTER DESIGN PARAMETERS. THE SWIRL ANGLES ARE GIVEN IN TIP, MID AND ROOT SECTIONS, RESPECTIVELY.

ψ_{R1}	0.299	ϕ_{R1}	0.477	π_{Stage1}	1.516
ψ_{R2}	0.284	ϕ_{R2}	0.452	π_{Stage2}	1.410
ψ_{R3}	0.273	ϕ_{R3}	0.515	π_{Stage3}	1.312
α_{IGV}	(18,10,0)	$M_{Tip,Rel,R1}$	1.192		
α_{S1}	(18,18,18)	$M_{Tip,Rel,R2}$	1.082		
α_{S2}	(20,20,20)	$M_{Tip,Rel,R3}$	0.971		
α_{S3}	(0,0,0)				

practices.

For the lightly loaded design studied here, it was possible to find a design that had a de Haller number above 0.72 for all stages and radii (11 stream lines were used). Maximum diffusion factors were set to 0.45. Axial Mach numbers were designed by adjusting the annulus definition to result in flow factors consistent with the computed stage loadings. Since the resulting stage loadings were in the range 0.27-0.30, see Table 2, flow factors in the range of 0.45-0.55 were deemed suitable. The resulting key design variables are summarized in Table 2. Stage loadings ψ and flow factors ϕ are at the inlet of the rotor blade mids. Stagnation pressure ratio is kept constant along the blade span to ensure a hub-strong design, believed to have the potential to give a good performance and surge margin.

The initial booster corner points are given in Table 3. The corner points and the initial design data are now transferred to the AxCent software for profiling and stage by stage CFD design.

TABLE 3. INITIAL BOOSTER CORNER POINTS

	r-coordinate	x-coordinate
$R_{1,tip}$	0.614	1.6031
$R_{1,hub}$	0.496	
$R_{2,tip}$	0.593	1.6966
$R_{2,hub}$	0.496	
$R_{3,tip}$	0.557	1.7810
$R_{3,hub}$	0.476	
$R_{3,exit,tip}$	0.532	1.8538
$R_{3,exit,hub}$	0.456	

CFD Based Throughflow Design

The detailed throughflow design was carried out in the design suite by Concepts NREC, using the programs AxialTM and AxCentTM. The first program (AxialTM) is a reduced order throughflow while the second (AxCentTM) is a time-marching throughflow program. The fundamental design was discussed in the previous section, and most general features were carried into the detailed throughflow design. The full engine design set the framework for certain key geometrical parameters, such as radial coordinates. The row chords were modified in order to arrive at more suitable aspect ratios (AR). The selection of aspect ratios is one of the very fundamental features of the compressor's design because it controls the length and ramp angles.

The total pressure levels at all rotor exits were retained at 72.855, 102.77 and 135.07 kPa from the initial throughflow design in SC90C. The row exit pressures mentioned and the basic

geometrical features resulted in the stage features shown in Table 4. At this point, a multiple circular arc (MCA) blade definition has been obtained for all stages, and the Mach number distribution from the calculations in AxCent™ of the compressor at the design point is shown in Fig. 3. A comparison with Grieb [16] shows that the fundamental stage parameters are within the conventional range for geared boosters.

It is convenient to plot the basic stage parameters in a ψ versus ϕ plot for a direct comparison with other useful stage parameters such as the deHaller- and throttling number, as shown

TABLE 4. PERFORMANCE CHARACTERISTICS OF THE THREE STAGES

Stage	Stage #1	Stage #2	Stage #3
ψ	0.29	0.28	0.27
ψ^1 [16]	0.3–0.4	0.3–0.4	0.3–0.4
ϕ	0.41	0.49	0.58
ϕ [16]	0.45–0.55	0.45–0.55	0.45–0.55
deHaller no.	0.74/0.92	0.75/0.97	0.76/0.88
Throttling no.	1.7	1.2	0.8
Throttling no. [16]	0.9–1.5	0.9–1.5	0.9–1.5
Stage π	1.5	1.4	1.3
Blade speed [m/s]	364	358	342
AVDR ²	1.21	1.19	1.13
η_p^3	0.9259	0.9290	0.9031

¹ Not to be seen a firm design rule - used as a general recommendation

² Should preferably be below 1.2...1.25

³ Koch & Smith loss model [17]

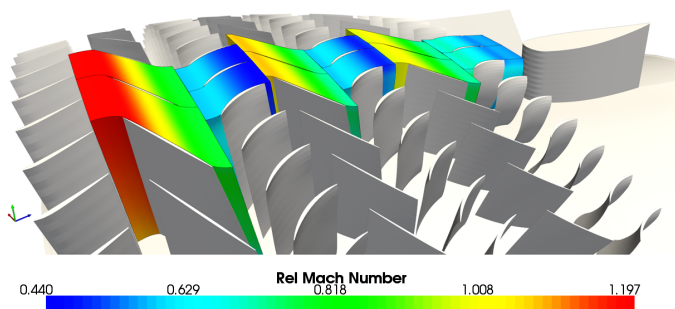


FIGURE 3. 3D VIEW OF THE RELATIVE MACH NUMBERS IN THE THREE STAGES.

in Fig. 4 where the stage values are represented by the yellow squares. The two lines denoting $|\beta| + \alpha = 90^\circ$ are related to the effective dynamic pressure factor (F_{EF}) in the stability model by Koch [18]. Higher values (*i.e.* to the left of the lines) impose higher stage stability because of the local higher dynamic head in to the subsequent row. The area enclosed by the solid blue lines represents a section of the plot that compressor stages commonly end up in.

As mentioned earlier, the selection of row aspect ratios is one of the very fundamental design features of the compressor. The compressor has values of 1.2, 1.3 and 1.2 for the first, second and third rotors, respectively. The corresponding numbers for the stators are 1.9, 1.6 and 1.3. This means that the booster is shorter than the version obtained in the previous design phase. The new compressor layout is shown in a meridional view in Fig. 5. The common definition of a low-AR stage is lower than two and the same for a high-AR stage is four. Hence, all rows for the compressor can be considered as low-AR. It is commonly accepted [19] that low-AR designs have the following pros:

- More rugged (or higher durability)
- Lower part count
- Lower cost
- Small change in weight
- Little change in length (higher stage loading)
- Normally better efficiency lower end-wall loading and $L/g2$, where L is the blade span and $g2 = s \cos(\beta)$
- Better stall resistance cf. directly above

Wennerstrom discusses further aspects of AR in [20] and [21], and one important conclusion is that losses associated with the passage shock are lower for designs with low aspect ra-

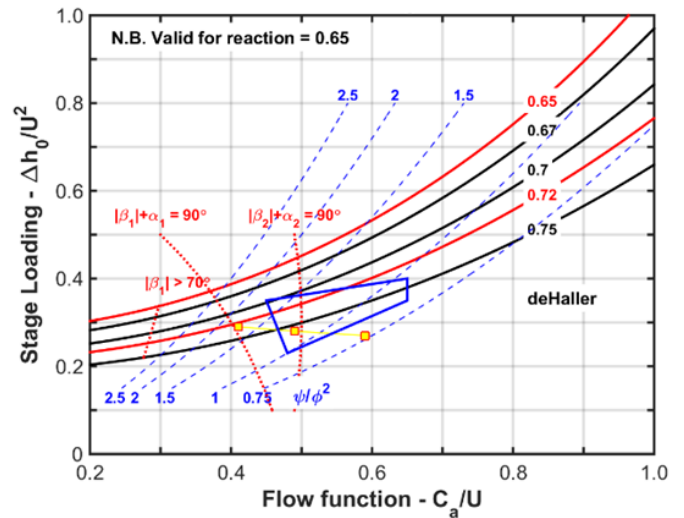


FIGURE 4. ROTOR LOADING CHART

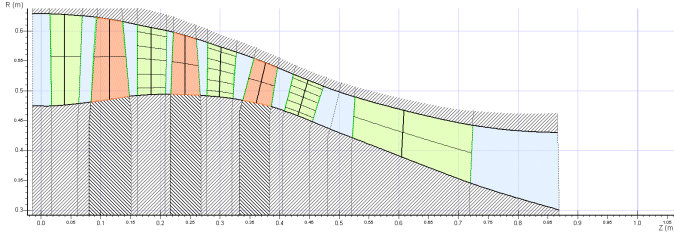


FIGURE 5. MERIDIONAL VIEW OF THE END-WALLS, THE VIGV, THE THREE STAGES AND THE DOWNSTREAM STRUT.

TABLE 5. THE SKOCH PARAMETER AND ASPECT RATIOS BASED ON TRUE AND AXIAL CHORD.

Stage #	Rotor		Stator		Stage Skoch - SP
	Chord	Axial chord	Chord	Axial chord	
1	1.22	2.26	1.90	2.11	2.3
2	1.30	2.02	1.57	1.76	3.0
3	1.20	1.67	1.33	1.36	2.9
Ref. [16]		1.6–2.7		1.6–2.7	
Ref. [22]					1.3–2.0

tios. The reason for this is that most shock loss models assumes 2D shock structures, which is not the case for low-AR designs. In addition to the shock losses, there are several positive knock-on effects such as higher Reynolds numbers, lower tip clearance to chord ratio, lower blade thickness to chord ratio, etc. The thicker end-wall boundary layers may increase the end-wall loss but the lower end-wall loading will improve the stall resistance.

The selected design values are shown in Table 5 together with the typical values from Grieb [16]. The Skoch-parameter is shown in the table, where it is indicated that the values are slightly higher than the normal range. This is an effect of the rather low stage loading and shows that the stages can be considered conventional. The solidity is typically set to give the right balance between the tangential blade force and the amount of wet surface. Too low a value will increase the profile loss since an increase in the required force per blade is associated with a "steeper" diffusion process on the suction side. Too high a solidity, on the other hand, will increase the amount of wet (actually rubbed) surface. The actual value is the outcome of the optimization of the compressor, but two typical approaches are: (1) set the tip solidity to the same value as for the relative inlet Mach number or (2) based on a certain diffusion factor. The initial setting is only set as an initial value for the profiling phase.

The spanwise distributions are set for constant total pressure and for specified absolute angle distributions after the rotors and stators, respectively. The aim of the design was to achieve a classic hub-strong design for optimum performance and surge margin. The design obtained at this point in the design process is referred to as the VINK compressor.

3D OPTIMIZATION

Optimization algorithm

The first stage of the VINK compressor is improved by 3D optimization using a Genetic Algorithm (GA) called the Non-dominated Sorting Genetic Algorithm II (NSGA-II) [23]. The GA mimics evolution in nature, representing the variable values by what is referred to as a chromosome. The algorithm works generation by generation, improving designs by crossover based on tournament selection and randomly changing individuals in a process referred to as mutation. In the tournament selection, the fitness of two individuals is compared and given a certain probability, the winner or loser will have a chance to pass on part of its chromosome to a new individual. For a single objective optimization, the fitness value would be based on the objective function. For a multi-objective optimization, the designs are split into different ranks, illustrated in Fig. 6 for two objective functions that should be maximized. In the figure, rank 1 designs consist of all designs that are not dominated by any other, *i.e.* no better designs exist with a higher value of both objective functions. All rank 1 designs can be considered to be non-dominated individuals and make up the Pareto front for the dataset. Another selection can be made of individuals that are only dominated by rank 1 designs, these will be designs of rank 2. This process can be repeated until all designs have been assigned a rank. This ranking is used as the fitness value in the multi-objective optimization.

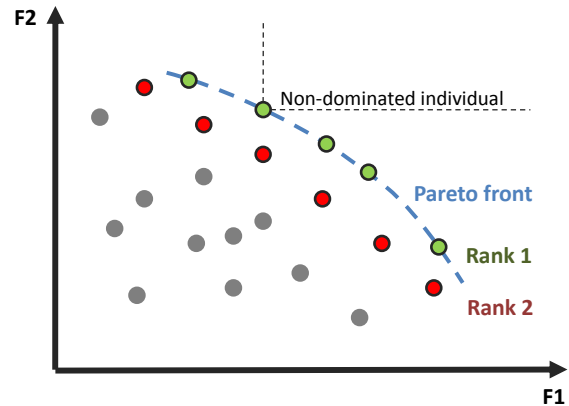


FIGURE 6. ILLUSTRATION OF A PARETO FRONT AND INDIVIDUALS OF DIFFERENT RANK

Mutation, where a part of the chromosome randomly change, is very powerful in terms of escaping local maxima of the objective function. Elitism is also used, which means that some of the best individuals of each generation are preserved for the next.

Optimization set-up

The optimization is done using two objective functions, maximizing the polytropic efficiency at the design point and maximizing the surge margin at design rotational speed. At the start of the optimization, 200 individuals are produced by latin hypercube sampling (LHS) of the design space. These are evaluated using 3D CFD calculations, and the objective functions are evaluated for each individual. The dataset is then used to build response surfaces. The response surface used is a radial basis function (RBF), which was shown in [24] to work well in combination with a GA for finding high performance compressor blade designs. In the present study, seven designs are then selected based on the optimization made on the RBF to be evaluated using CFD. The selection is made of rank 1 individuals evenly spaced along the Pareto front, including the designs with the maximum value of each objective function, *i.e.* the "end-points" of the Pareto front. Three additional designs are chosen to explore the design space in areas where the uncertainty of the response surface may be large. This is done by a Lipschitz sampling algorithm described in [25], where the distance in the design space to known designs and the change in an objective function (polytropic efficiency) in that part of the design space, are considered. However, this selection process suffers from the curse of dimensionality. Out of the 18 design variables (described in the next section) used in the present study, 6 variables that are determined to have the largest impact on the objective function are selected and used for the Lipschitz sampling algorithm.

One optimization on the response surface and a subsequent evaluation of selected designs using CFD is referred to as a design iteration. The process is repeated until the Pareto front is considered converged, typically within 5–25 design iterations when 18 design variables are used, depending on the variable range permitted and number of samples used for the initial LHS.

Variables

The variables used for the 3D optimization are the leading and trailing edge blade angles and a variable influencing the camber distribution at 0%, 50% and 100% span on both the rotor and the stator. The variation in blade angles influences the local stagger angle. The axial chord is kept constant, resulting in the true chord length being influenced by the design changes. The profile thickness is set as a fraction of the axial chord length, so that the blade thickness in terms of the absolute value is kept con-

stant. The variable limits used in the optimization are extended if the maximum value of a variable relative to the allowed variable range is favored during optimization. In this way, an optimum can be found that is not at the boundary of the allowed variable range.

Requirements

The requirements put on the stage are based on those specified in the earlier design phase. The stage should be able to operate close to the specified design point (a corrected mass flow of 89.52 kg/s and a total-to-total pressure ratio of 1.51) in the compressor map, and the swirl angle from the stator should be similar to the design intent in the earlier design phase since the preliminary design of the next stage was attained considering this flow field. The maximum allowed deviation of the swirl angle from the specified profile in the spanwise range 5-95% is set to 2 degrees. The maximum allowed deviation of the average swirl angle from the design intent is set to 1 degree.

A requirement was placed on the surge margin (SM) to be a minimum of 10% at design rotational speed. The surge margin is defined as shown in Eq. 1 and is based on the throttle area at the design point and the throttle area at the last stable operating point.

$$SM = 1 - \frac{A_{last\ stable\ operating\ point}}{A_{design\ throttle}} \quad (1)$$

The last stable operating point for a given design is taken as the operating point for which the peak static pressure recovery coefficient, C_p , defined in Eq. 2, is achieved in either the rotor or the stator. The variable $\bar{p}_{01,rel}$ denotes the average relative total pressure at the inlet, and the variables \bar{p}_1 and \bar{p}_2 denote the average static pressure at the inlet and outlet of the domain being evaluated, respectively.

$$C_p = \frac{\bar{p}_2 - \bar{p}_1}{\bar{p}_{01,rel} - \bar{p}_1} \quad (2)$$

Geometry

The geometry denoted R1S1A is a fit of the MCA definition of the first rotor and stator from AxCentTM, obtained using an airfoil profiling tool. The tip clearance has not been considered.

Numerical

The CFD calculations are made in the in-house code Volsol++ developed by GKN Aerospace and Chalmers. Volsol++ is a density-based, finite-volume solver using a three-stage Runge-Kutta time marching method. The turbulence model used is the realizable $k - \varepsilon$ model with the Kato-Launder limiter. Wall

boundaries have been treated as adiabatic, and wall functions have been used to resolve the boundary layers. All simulation results presented herein have been run as steady state. A single rotor and stator passage is used for the calculations, using a periodic boundary condition to account for the number of blade passages. The interface between the rotor and stator is specified as a mixing plane [26].

The inlet boundary condition is specified in terms of total pressure, total temperature, turbulence kinetic energy, turbulent dissipation and the direction of the velocity vector. The turbulence intensity was set to 5% and the turbulent length scale was specified as 1 mm. The radial distribution of total temperature, total pressure and the velocity vectors at the inlet was obtained from the calculations made in the earlier design phase. A non-reflective boundary condition is used at the outlet [27]. Transition is not modeled, and the flow is considered fully turbulent on all surfaces.

The computational grid is made up of hexahedral elements. The boundary layer is resolved using an O-grid, while the blade passage domain is constructed using H-type blocks. Five com-

putational grids, listed in Table 6, were considered in the mesh study. The performance variation of R1S1A for the five mesh sizes is illustrated in Fig. 7. The polytropic efficiency, which is one of the most sensitive performance parameters to the grid size, differs 0.15% from the medium mesh to the very fine mesh for operating points along the operating line, and 0.05% from the fine to the very fine mesh. The predicted corrected mass flow and total pressure ratio along the operating line differ at most 0.05% from the medium to the very fine mesh, and below 0.05% from the fine to the very fine mesh. For a throttle line close to surge the difference in predicted corrected mass flow and total pressure from the medium to the very fine mesh is in the range 0.15–0.20% and for polytropic efficiency the difference is 0.30%. From the fine to very fine mesh the performance parameters differs by approximately 0.10%.

It is concluded from the mesh study that the mesh size denoted as medium in Table 6 is an appropriate mesh size to use for optimization, and the mesh denoted as fine is appropriate for use for a final performance evaluation after optimization. The mesh sizes medium and fine will be referred to in the remainder of the paper as the Design mesh and the Verification mesh, respectively.

TABLE 6. MESH SIZES USED IN THE MESH STUDY

Mesh	Rotor cells	Stator cells	Comment
Very coarse	27k	26k	-
Coarse	52k	52k	-
Medium	105k	102k	Design mesh
Fine	204k	205k	Verification mesh
Very fine	399k	395k	-

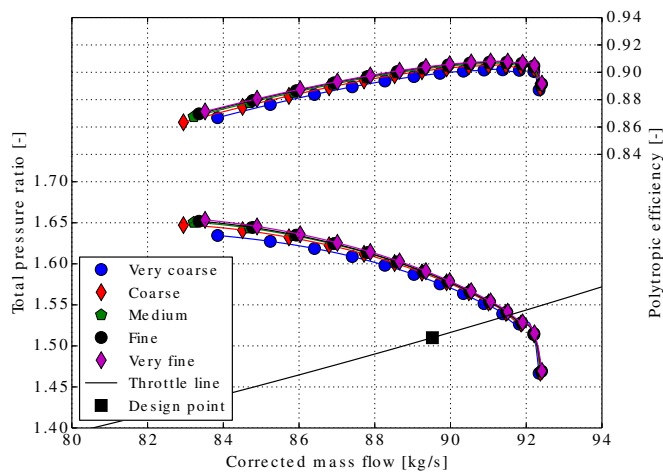


FIGURE 7. PERFORMANCE INFLUENCE BY MESH SIZE

New first stage design

During optimization, the design of interest was the design with the highest efficiency that also met all design requirements. The best design that was eventually chosen for further evaluation was found in 16 design iterations. Twelve additional design iterations were run without finding a better design.

Once a new design has been obtained, the next step is to verify the performance using the Verification mesh. The speedline of the optimized stage (R1S1B) is shown in Fig. 8, including the performance of the original first stage (R1S1A) using the same mesh size. The predicted polytropic efficiency of the operating point closest to the throttle line for each design increased from 90.7% for R1S1A to 91.0% for R1S1B. The difference in mass flow at the same operating points compared to the design point decreased from approximately 2.2% to 0.25%. The surge margin criterion, illustrated as a throttle line representing a 10% surge margin in Fig. 8, is shown to be fulfilled. With the definition used in the present study, the surge margin is calculated to be 15.8% and 16.6% for R1S1A and R1S1B, respectively.

The maximum and mean deviation of the stator exit swirl angle (in the range 5–95% span) from the design intent is listed in Table 7. The swirl angle evaluation is done for operating points along the throttle line that pass through the design point. The radial distribution of the swirl angle is illustrated in Fig. 9, and it is shown that R1S1A was already relatively close to the design intent but has been further improved to be within the criteria of a maximum allowed deviation of 2° for the new design.

The radial loading distribution of the rotor before and after optimization is illustrated in Fig. 10 as the total pressure and total

temperature increase at different spanwise positions. The overall loading of the rotor blade has been reduced, as a lower total pressure ratio is required at the same operating speed for the new design. It is also shown that the tip has been off-loaded relative to the rest of the blade for the new design. It would be expected that losses in the tip region would decrease by off-loading the tip. To evaluate the radial distribution of loss, a loss coefficient ω defined as shown in Eq. 3, is used to show the difference in loss for the two rotor geometries.

$$\omega = \frac{p_{02,rel} - p_{01,rel}}{p_{01,rel} - p_{1,rel}} \quad (3)$$

The radial variation of ω is shown for the two rotors to the left in Fig. 11, and it is shown that the value of omega is overall lower for R1S1B from 0-70% span, but higher from 70-100% span. The incoming dynamic pressure is lower in the tip region (and overall) for the new design due to the lower loading, which contributes to a higher value of the loss coefficient but a difference in total pressure loss exist in the tip region, even if this is accounted for. The increase of losses in the tip region is believed to be due to a longer true chord in the tip region for the new blade, shown to the right in Fig. 11, increasing friction drag. As the axial chord is kept constant in the optimization, a decrease in blade

loading (increase in stagger) results in a longer true chord. Altering the true chord length of the rotor is an approach that could result in an additional reduction of loss for the rotor. Mach number contours are shown to illustrate the flow field at 90% span for designs R1S1 and R1S1B span in Fig. 12.

The geometries of R1S1A and R1S1B are illustrated at three spanwise positions in Fig. 13. It shows the longer true chord of R1S1B in the tip region as the stagger angle was increased. A change of the stator geometry is also shown, where the leading edge blade angle has been altered to match the flow that exits the new rotor geometry. A change of the stator trailing edge blade angle has been made to attain the specified radial swirl distribu-

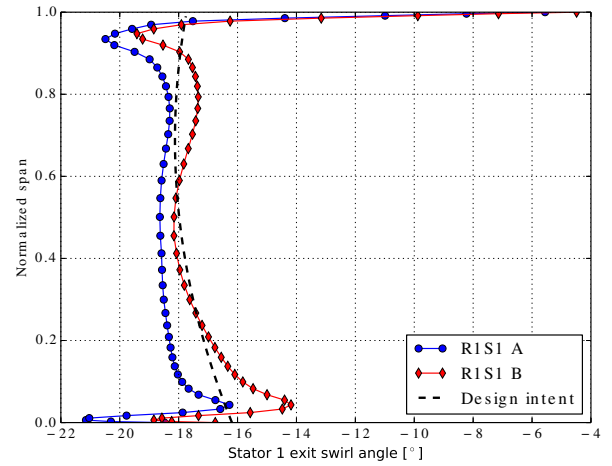


FIGURE 9. RADIAL SWIRL ANGLE VARIATION FROM STATOR 1 AT THE DESIGN POINT

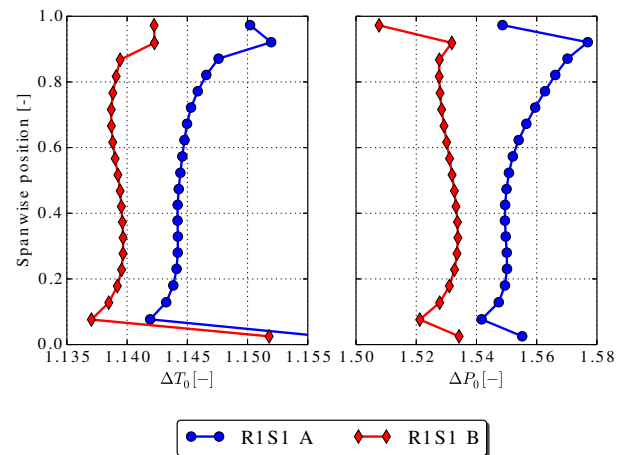


FIGURE 10. INCREASE IN TOTAL TEMPERATURE AND TOTAL PRESSURE OVER THE ROTORS

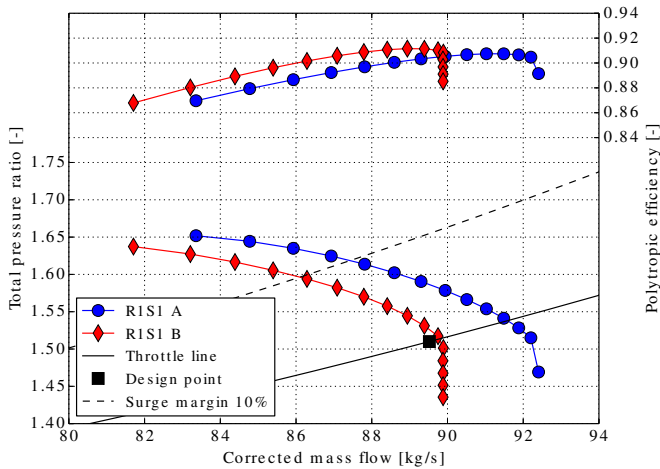


FIGURE 8. COMPRESSOR STAGE PERFORMANCE BEFORE (R1S1 A) AND AFTER (R1S1 B) OPTIMIZATION

TABLE 7. SWIRL ANGLE DEVIATION FROM DESIGN INTENT

Design	Mean swirl dev.	Max swirl dev.
R1S1 A	0.7°	2.5°
R1S1 B	0.3°	1.7°

tion from the stator to the next stage.

With the optimized stage R1S1B, the performance and out-flow angles are now close to those used to define the MCA geometries of stage 2 in the previous design step. Using this as the new first stage increase the probability of subsequent stages performing close to their predicted performance from the through-flow calculations.

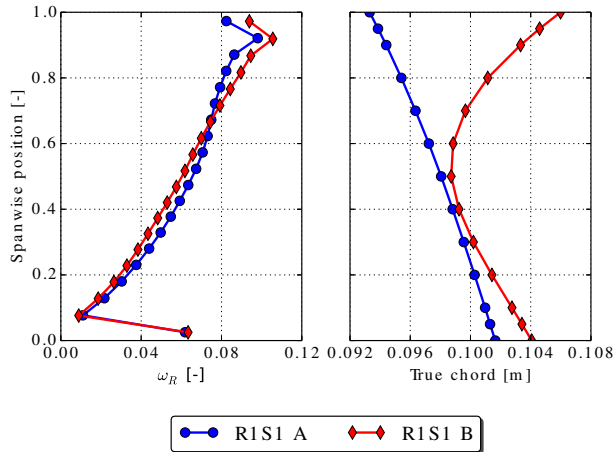


FIGURE 11. LOSS COEFFICIENT AND TRUE CHORD LENGTH FOR THE ROTOR BLADES

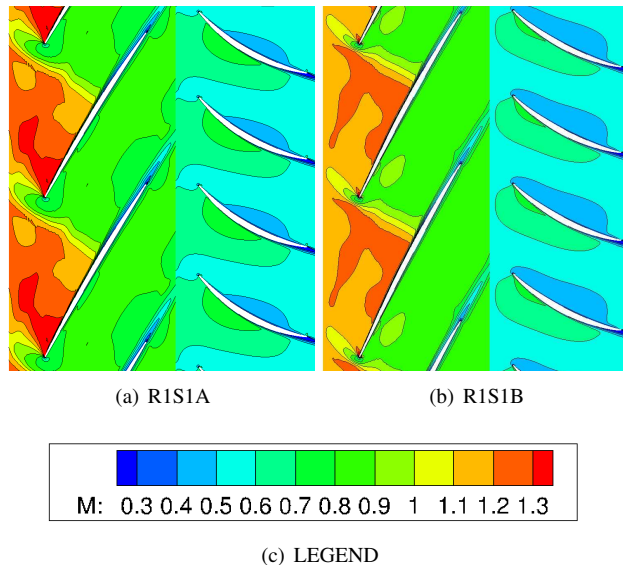


FIGURE 12. MACH NUMBER CONTOURS AT 90% SPAN FOR OPERATING POINTS ALONG THE THROTTLE LINE THAT PASS THROUGH THE DESIGN POINT

AEROMECHANICAL ASSESSMENT

Following the aerodynamic 3D optimization, the aeromechanical analyses were performed to assess the aero-optimized rotor blades in the first stage of the compressor. Starting from the aero-optimized geometry, denoted as the "hot" geometry, the first step involves "un-running" of the blades to obtain the so called "cold" blade geometry *i.e.* the geometry of the blade at a stand-still. This "hot-to-cold" geometry transformation is an iterative process, carried out using the ANSYS FE solver. The static structural analyses were thereafter performed on the derived cold geometry in order to assess the blade strength under the centrifugal, aerodynamic and thermal loads at the design point. The blades were modelled using quadratic 3-D 20-node solid elements (ANSYS elements SOLID186), with the domain containing a total of 7.7K elements and 35.7K nodes. The motion of the blade is imposed as a moving mesh boundary condition and the grid points are allowed to slide along the casing. The material chosen for the rotor blades was Titanium alloy Ti-6Al-4V. The estimated maximum static stress levels on the blades under consideration were well below the ultimate tensile strength of the chosen material.

The pre-stressed blades were then subjected to modal analysis to produce the blade mode shapes. In this initial analysis, the blade only modes were considered *i.e.* the disk was not included. Potential resonance crossings originating from the blade row interaction were mapped in a Campbell diagram over the entire operating range of the booster (60% to 115% of the design point rotational speed). The potential resonance conditions occur when the excitation frequencies (engine order lines) coincide with the eigen-frequencies of the blades. Fig. 14 indicates that, for the first stage rotor blades, no dangerous resonance crossings could be identified for the lower mode shapes. The blade count in each

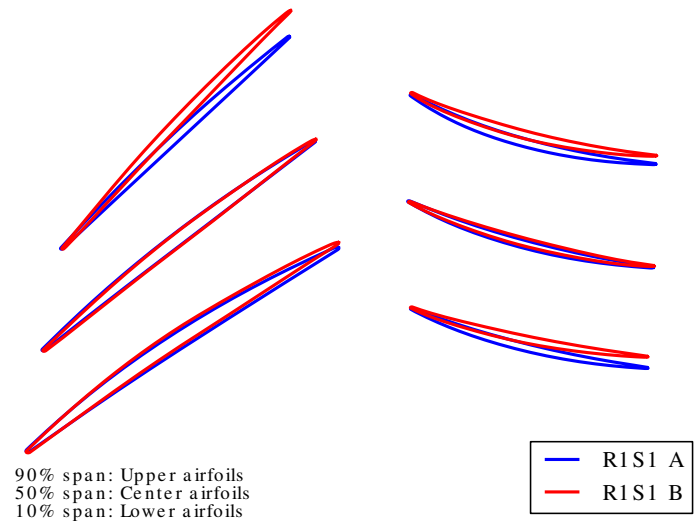


FIGURE 13. AIRFOIL PROFILES

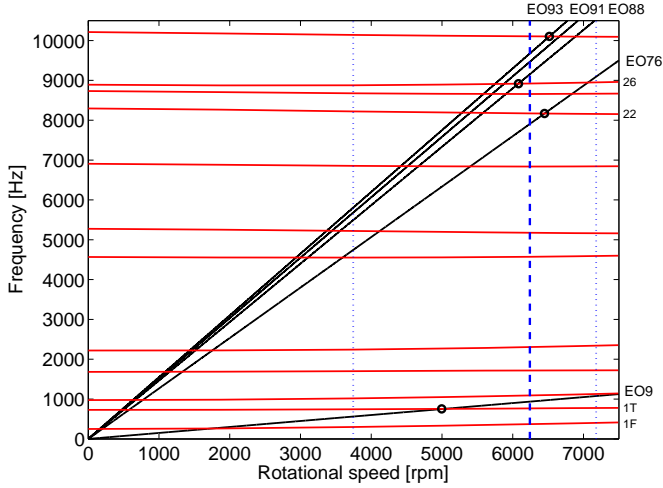


FIGURE 14. CAMPBELL DIAGRAM FOR STAGE 1 ROTOR BLADES (R1)

blade row is listed in Table 8. The EO9 line, corresponding to the 9 ICC struts located in the downstream duct between the booster and HPC, crosses the mode 2 line at about 80% of the design rotational speed, but, considering that the position of the ICC struts is far downstream from rotor 1, the aerodynamic influence of these can be neglected. The potential dangerous crossings resulting from the adjacent blade row interaction might occur at higher frequencies and involve higher order mode shapes *e.g.* crossings for modes 22 and 26 indicated in the diagram. Determination of how critical the levels of these resonance crossings are will not be considered within the scope of this paper, but will be addressed further at a later stage of the compressor aeromechanical design.

To assess the flutter stability of the rotor blades, aerodynamic damping predictions were carried out for the two lowest mode shapes (1st flex 1F and 1st torsion 1T). The aerodynamic damping is due to the unsteady flow forces acting on the blades produced by the blades' vibration. Considering the low structural damping of a blisk configuration of the rotor, aerodynamic damping predictions are a crucial component of the aeromechanical design chain. The aerodynamic damping calculations were carried out using the RPMTurbo LUFT code. The code is capable of performing steady-state flow simulations and linearized unsteady flow simulations. The flow model used by the code is the 3D URANS flow equations with the Spalart-Allmaras turbulence

TABLE 8. VINK COMPRESSOR BLADE COUNT

VIGV	R1	S1	R2	S2	R3	S3	ICC
76	51	88	69	93	72	91	9

model, fully linearized for the unsteady flow simulations. The code has previously been validated for flutter analysis [28–30]. A 3D non-reflecting boundary condition was applied at both the inlet and outlet boundaries.

Similar to the above described CFD calculations, the flow domain for the initial steady state solution contained one rotor and one stator passage. The computational grid used was of multi-block type containing both O- and H-blocks, and the entire computational domain consisted of 876K hexahedral volume elements with 920K nodes. The boundary layers were resolved using an O-grid with mean y^+ values < 4 . Only the rotor domain was considered for flutter simulations.

In linearized flow solvers, the unknown unsteady flow perturbations are assumed to be harmonically oscillating about their steady-state values. The resulting linearized solution gives the amplitudes and phase of the flow perturbations throughout the flow domain. The aerodynamic damping coefficient Ξ was calculated to assess the flutter stability of the blades [31]. The parameter presents the negative aerodynamic work per cycle W_{aero} normalized with the oscillation amplitude

$$\Xi = \frac{-W_{aero}}{\pi L h_{max}^2 p_{ref}} \quad (4)$$

where L is the length of the blade, h_{max} is the maximum blade mode shape amplitude and $p_{ref} = p_0 - p_1$ is the reference dynamic head, where p_0 is the average relative total pressure and p_1 is the average static inlet pressure. The unsteady aerodynamic work per cycle on the blade can be found by integrating the pressure on the blade surface with blade displacement. Positive aerodynamic damping values indicate a stable condition *i.e.* no flutter.

Fig. 15 and Fig. 16 show the aerodynamic damping curves (S-curves) for the 1F and 1T mode. The aerodynamic damping was calculated for both the reference (case A) and the aero-optimized blade geometries (case B). The reduced frequency k for the investigated modes for the aero-optimized blade was as follows: $k=0.619$ for 1F mode and $k=1.281$ for 1T (here, the reduced frequency is based on the full chord). The corresponding values for the reference geometry were: $k=0.627$ for 1F mode and $k=1.349$ for 1T. The relative Mach number at the inlet of the rotor domain was $M1=1.1328$ (case A) and $M1= 1.1303$ (case B).

It can be seen from Fig. 15 that the aerodynamic damping curves for the first bending mode 1F are rather similar for both geometries. The least stable mode is located at ND 3 and has an aerodamping coefficient of 0.094, which is a relatively small value. However, the rotor blades remain stable (positive aerodynamic damping) for all nodal diameters of the travelling wave mode.

The aerodamping curves for the 2nd mode (1T) are shown to be slightly more different from each other when comparing

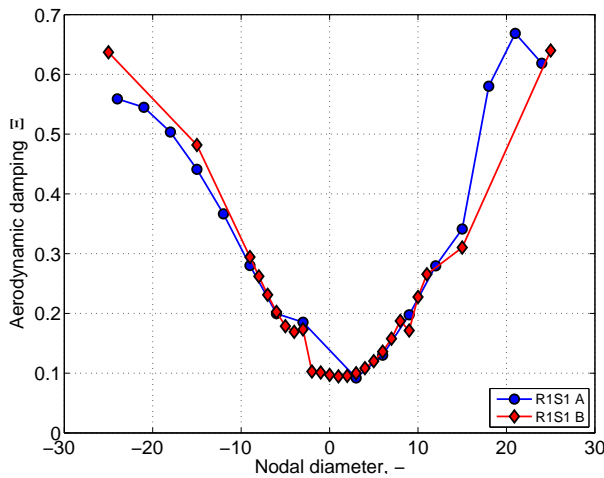


FIGURE 15. AERODYNAMIC DAMPING CURVE FOR MODE 1 (1F)

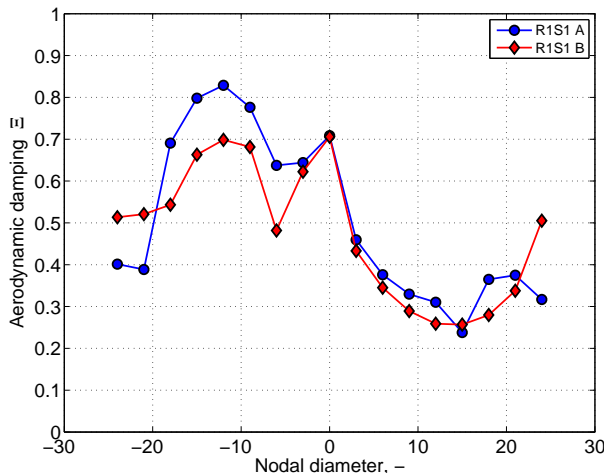


FIGURE 16. AERODYNAMIC DAMPING CURVE FOR MODE 2 (1T)

the reference and optimized blade. The peak-to-peak amplitude of the S-curve for the reference geometry is slightly higher. The blade oscillating frequency of the 1T mode for the optimized geometry is lower compared to the reference geometry (766Hz vs. 808Hz). The consequence of this is that the acoustic resonances that might be observed as sudden dips in the damping values occur at different positions. The damping value of the least stable mode has not changed significantly. As expected, based on the observed higher reduced frequency of the 1T mode, the aerodynamic damping values of the 1T mode are overall higher than for the 1F mode and the blade row remains stable for all nodal diameters.

SUMMARY

The present paper has described a multidisciplinary conceptual design of a three stage, high speed, high efficiency booster as part of a collaboration between three Swedish universities (Chalmers, KTH and LTH). The collaboration has shown the capability of performing the necessary steps leading to a 3D definition of a high speed compressor. A goal at the outset of the project was to make a publicly available geometry to be used for future studies. In accordance with this goal, the geometry and boundary conditions used for the present study are now publicly available at “github.com/nikander/VINK” [12].

The design phases are described, starting from basic aircraft and engine thrust requirements and ending with an aerodynamically optimized and structurally analyzed geometry. After defining the basic aircraft and engine thrust requirements, the interface points, location and overall performance data required of the booster were defined. A throughflow method was then used to define the initial corner points of the booster. In the next step, a CFD based throughflow design method was used to refine the shape of the hub and shroud-lines as well as to provide an MCA definition of the compressor blades. The design that was obtained after MCA profiling of the stages is referred to as the VINK compressor. The first stage of the compressor was then optimized using detailed CFD calculations to meet design criteria specified in the earlier design phases. Finally, the first stage was evaluated with respect to mechanical considerations.

The aerodynamically optimized first stage was shown to meet the design intent of the earlier design phases and to achieve a 91% polytropic efficiency at the design point. The aeromechanical assessment of the stage showed that the potential resonance crossings between excitations lines related to blade passing frequency will occur at rather high order modes, and, from a flutter stability point of view, both the original and the aerodynamically optimized rotor blades of the first stage behave similarly and are aerodynamically stable.

ACKNOWLEDGMENT

The authors would like to acknowledge the support and expertise provided by Hans Mårtensson and Lars Ellbrant at GKN Aerospace Engine Systems.

This work was funded by the Swedish National Aviation Engineering Research Programme, NFFP. The authors would like to acknowledge the financial support of VINNOVA, the Swedish Defense Material Administration (FMV) and GKN Aerospace. The authors would also like to thank the National Supercomputer Center, Linköping, Sweden and Chalmers Centre for Computational Science and Engineering, Gothenburg, Sweden for the computational resources required for this work.

REFERENCES

- [1] NRIA Flyg 2016, New challenges - and new solutions. <http://innovair.org/en/wp-content/uploads/2016/06/nriaflyg-eng-160601b-webb1.pdf>. Accessed: 2016-11-16.
- [2] Larsson, L., Grönstedt, T., and Kyprianidis, K., 2011. "Conceptual Design and Mission Analysis for a Geared Turbofan and an Open Rotor Configuration". In Proceedings of ASME Turbo Expo 2007, no. GT2011-46451.
- [3] Kurzke, J., 2009. "Fundamental Differences Between Conventional and Geared Turbofans". In Proceedings of ASME Turbo Expo 2009, no. GT2009-59745.
- [4] Bruce G. M., and Andy, B., 2012. "The Ultrafan Engine and Aircraft Based Thrust Reversing". In 40th Joint Propulsion Conference and Exhibit, no. AIAA Paper 2012-3919.
- [5] Grönstedt, T., Xisto, C., Sethi, V., Rolt, A., Rosa, N. G., Seitz, A., Yakinthos, K., Donnerhack, S., Newton, N., Schmitz, O., and Lundblad, A., 2016. "Ultra Low Emission Technology Innovations for Mid-Century Aircraft Turbine Engines". In Proceedings of ASME Turbo Expo 2016, no. GT2016-56123.
- [6] Gallimore, S. J., 1999. "Axial Flow Compressor Design". *Journal of Mechanical Engineering Science*, **213**(5), pp. 437–449.
- [7] Wisler, D. C., Koch, C. C., and Smith, L. H. Jr., 1977. Preliminary Design Study of Advanced Multistage Axial Flow Core Compressors. Tech. rep., NASA Lewis Research Center. NASA-CR-135133.
- [8] Yan, X., Takizuka, T., Kunitomi, K., Itaka, H., and K., T., 2008. "Aerodynamic Design, Model Test, and CFD Analysis for a Multistage Axial Helium Compressor". *Journal of Turbomachinery*, **130**(3), pp. 031018–1–031018–12.
- [9] Wadia A. R., Wolf D. P., and Haaser F. G., 2002. "Aerodynamic Design and Testing of an Axial Flow Compressor With Pressure Ratio of 23.3:1 for the LM2500+ Gas Turbine". *Journal of Turbomachinery*, **124**(3), pp. 331–340.
- [10] Sehra, A., Bettner, J., and Cohn, A., 1992. "Design of a High-Performance Axial Compressor for Utility Gas Turbine". *Journal of Turbomachinery*, **114**(2), pp. 277–286.
- [11] Dickens, T., and Day, I., 2010. "The Design of Highly Loaded Axial Compressors". *Journal of Turbomachinery*, **133**(3), pp. 031007–1–031007–12.
- [12] High Speed Booster Design Data. github.com/nikander/VINK. Uploaded: 2016-11-20.
- [13] Grönstedt, T., 2006. "Development of Methods for Analysis and Optimization of Complex Jet Engine Systems". PhD thesis, Chalmers University of Technology.
- [14] Xin, Z., Grönstedt, T., and Kyprianidis, K., 2013. "Assessment of the performance potential for a two-pass cross flow intercooler for aero engine applications". In 21st ISABE conference, no. ISABE Paper 2013-1215.
- [15] PCA Engineers Ltd, 2014. SC90C a stream line curvature program for axial compressors. Version 8-2.
- [16] Grieb, H., 2009. *Verdichter fr Turbo-Flugtriebwerke*. Heidelberg: Springer Verlag. ISBN: 978-3-540-34373-8.
- [17] Koch, C., and Smith, L., 1979. "Loss Sources and Magnitudes in Axial-Flow Compressors". *Journal of Engineering for Power*, **98**(3), pp. 411–424.
- [18] Koch C. C., 1981. "Stalling Pressure Rise Capability of Axial Flow Compressor Stages". *Journal of Engineering for Power*, **103**(4), pp. 645–656.
- [19] Johnson, R., 1998. *Handbook of Fluid Dynamics*. CRC Press. ISBN: 0-8493-2509-9.
- [20] Wennerstrom, A. J., 2000. *Design of Highly Loaded Axial-Flow Fans and Compressors*. White River Jct. ISBN: 0-933283-11-3.
- [21] Wennerstrom, A. J., 1989. "Low Aspect Ratio Axial Flow Compressors: Why and What it Means". *Journal of Turbomachinery*, **11**, pp. 357–365.
- [22] Laroselliere, L., Wood, J., Hathaway, M., Medd, A., and Dang, T., 2002. Aerodynamic Design Study of Advanced Multistage Axial Compressor. Tech. rep. ARL-TR-2859, NASA/TP.
- [23] Deb, K., Pratap, A., Agarwal, S., and Meyarivan, T., 2000. A Fast and Elitist Multi-Objective Genetic Algorithm: NSGA-II. Tech. rep., Indian Institute of Technology Kanpur. KanGAL Report No. 200001.
- [24] Ellbrant, L., Eriksson, L.-E., and Martensson, H., 2012. "CFD Optimization of a Transonic Compressor using Multiobjective GA and Metamodels". In 28th International Congress of the Aeronautical Sciences, no. 2012-4.6.3.
- [25] Lovison, A., 2010. "Adaptive Sampling with a Lipschitz Criterion for Accurate Metamodeling". *Communications in Applied and Industrial Mathematics*, **1**(2), pp. 110–126.
- [26] Stridh, M., 2006. "Modeling Unsteady Flow Effects in 3D Throughflow Calculations". PhD thesis, Chalmers University of Technology.
- [27] Engquist, B., and Majda, A., 1977. "Absorbing Boundary Conditions for the Numerical Simulation of Waves". *Mathematics of Computation*, **31**(139), pp. 629–651.
- [28] Petrie-Repar, P. J., McGhee, A. M., and Jacobs, P. A., 2007. "Three-dimensional Viscous Flutter Analysis of Standard Configuration 10". In Proceedings of ASME Turbo Expo 2007, no. GT2007-27800.
- [29] Petrie-Repar, P. J., McGhee, A. M., Jacobs, P. A., and Gollan, R., 2006. "Analytical Maps of Aerodynamic Damping as a Function of Operating Condition for a Compressor Profile". In Proceedings of ASME Turbo Expo 2006, no. GT2006-90829.
- [30] Petrie-Repar, P. J., 2010. "Three-dimensional non - reflecting boundary condition for linearized flow solvers". In Proceedings of ASME Turbo Expo 2010, no. GT2010-23335.
- [31] Verdon, J. M., 1987. Linearized Unsteady Aerodynamic

Theory. AGARD Manual on Aeroelasticity in Axial-Flow Turbomachines, Vol. 1, Unsteady Turbomachinery Aerodynamics, Chapter 2, AGARD-AG-298.